



Cite this: *Phys. Chem. Chem. Phys.*, 2017, 19, 17396

# Competition between the H- and D-atom transfer channels in the $\text{H}_2\text{O}^+ + \text{HD}$ reaction: reduced-dimensional quantum and quasi-classical studies

Hongwei Song,  <sup>a</sup> Anyang Li,  <sup>b</sup> Minghui Yang  <sup>a</sup> and Hua Guo  <sup>c</sup>

The ion–molecule reaction between a water cation and a hydrogen molecule has recently attracted considerable interest due to its importance in astrochemistry. In this work, the intramolecular isotope effect of the  $\text{H}_2\text{O}^+ + \text{HD}$  reaction is investigated using a seven-dimensional initial state-selected time-dependent wave packet approach as well as a full-dimensional quasi-classical trajectory method on a full-dimensional *ab initio* global potential energy surface. The calculated branching ratios for the formation of  $\text{H}_3\text{O}^+$  and  $\text{H}_2\text{DO}^+$  via H- and D-transfer agree reasonably well with the experimental values. The preference to the formation of the  $\text{H}_3\text{O}^+$  product observed using the experiment at low collision energies is reproduced by theoretical calculations and explained by a one-dimensional effective potential model.

Received 3rd May 2017,  
Accepted 6th June 2017

DOI: 10.1039/c7cp02889j

rsc.li/pccp

## 1. Introduction

Ion–molecule reactions play an important role in many areas of chemistry.<sup>1</sup> Detailed information on ion–molecule reactions can provide an in-depth understanding of the chemical composition of interstellar gas clouds,<sup>2</sup> planetary ionospheres,<sup>3</sup> and electric discharges.<sup>4</sup> Ion–molecule reactions are partly responsible for enhanced D-to-H ratios in various interstellar molecules and thus can be used to interpret cosmic origins and abundances of interstellar molecules.<sup>5,6</sup> The reaction between a water cation ( $\text{H}_2\text{O}^+$ ) and a hydrogen molecule ( $\text{H}_2$ ) represents one of the most important ion–molecule reactions occurring in interstellar media due to the high abundance of both reactants in astrochemical environments.<sup>7–9</sup> Indeed,  $\text{H}_3\text{O}^+$  and its deuterated isotopomers have been recently detected by the powerful Herschel Space Observatory in various regions of the outer space. Since these isotopomers are thought to be observable in the core of dense clouds immediately prior to protostar formation, they serve as kinematic tracers for probing the velocity structure.<sup>10–13</sup> The water cation is also a prototypical proton acceptor, producing

the hydronium ion ( $\text{H}_3\text{O}^+$ ) that is crucial to studying chemical dynamics and acid catalysis in aqueous solutions.<sup>14</sup>

Due to the significance of the title reaction in astrochemical models, the rate coefficients of the title reaction have been measured over a wide range of temperatures.<sup>15–23</sup> The obtained gas-kinetic rate coefficients indicated that the  $\text{H}_2\text{O}^+ + \text{H}_2$  reaction is a barrierless reaction. However, the latest experimental study of the temperature effect suggests the existence of a small reaction bottleneck.<sup>23</sup> Using a novel sequential scheme of the vacuum ultraviolet (VUV) pulsed field ionization-photoion (PFI-PI) technique, Ng and his coworkers have achieved rovibrational-state selection in generating the reactant  $\text{H}_2\text{O}^+$  ions with a narrow laboratory kinetic energy range.<sup>24</sup> This advance has enabled the study of the translational, rotational, and vibrational energy effects on the chemical reactivity of  $\text{H}_2\text{O}^+(X^2B_1)$  in collision with  $\text{H}_2$ ,  $\text{D}_2$  and HD.<sup>24–28</sup> These authors have measured absolute integral cross sections by implementing the  $\text{H}_2\text{O}^+$  PFI-PI ion source with a double-quadrupole–double-octopole (DQDO) apparatus. Surprisingly large enhancement of the reactivity by rotational excitations of the  $\text{H}_2\text{O}^+$  reactant was detected at low collision energies.<sup>24,27,28</sup> In addition, strong intra- and intermolecular isotope effects have been observed.<sup>25,26</sup>

To provide a better understanding of the kinetics and mode specific dynamics of the  $\text{H}_2\text{O}^+ + \text{H}_2$  reaction and its isotopic substitutions, Li *et al.* recently developed an accurate full-dimensional global potential energy surface (PES),<sup>29</sup> which consists of a short-range strong interaction PES and long-range electrostatic terms, connected with a switching function. The former was fit to  $\sim 81\,000$  *ab initio* points in the interaction region at the explicitly correlated unrestricted coupled cluster

<sup>a</sup> Key Laboratory of Magnetic Resonance in Biological Systems, State Key Laboratory of Magnetic Resonance and Atomic and Molecular Physics, National Center for Magnetic Resonance in Wuhan, Wuhan Institute of Physics and Mathematics, Chinese Academy of Sciences, Wuhan, 430071, China.

E-mail: hwsong@wipm.ac.cn

<sup>b</sup> College of Chemistry and Materials Science, Northwest University, Xi'an, 710069, China

<sup>c</sup> Department of Chemistry and Chemical Biology, University of New Mexico, Albuquerque, New Mexico, 87131, USA

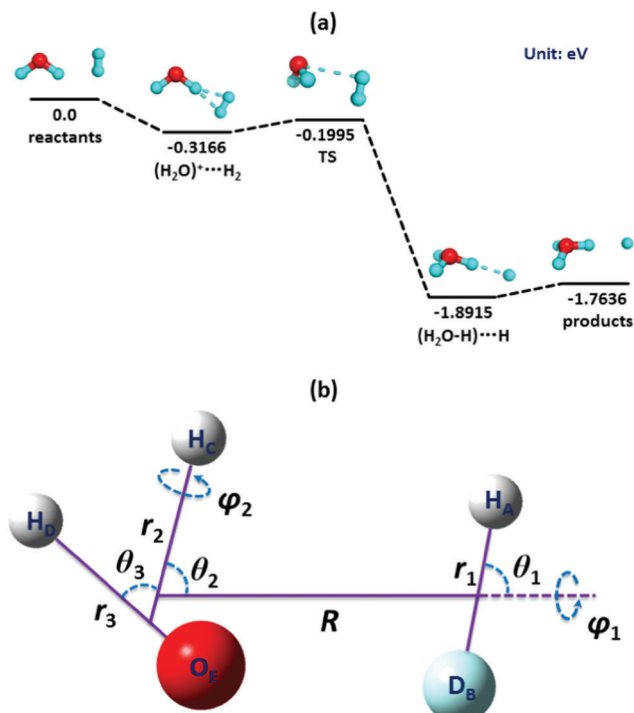


Fig. 1 (a) Schematic diagram of the reaction path for the  $\text{H}_2\text{O}^+ + \text{H}_2 \rightarrow \text{H}_3\text{O}^+ + \text{H}$  reaction. (b) The nine-dimensional Jacobi coordinates for the AB + CDE system in the reactant frame. In the reduced seven-dimensional model,  $r_2$  and  $r_3$  are fixed at their corresponding equilibrium distances.

single, double and perturbative triple level with the augmented correlation-consistent valence polarized triple zeta basis set (UCCSD(T)-F12b/aug-cc-pVTZ), using the permutation invariant polynomial neural network approach.<sup>30</sup> On the other hand, the long-range interactions in the reactant asymptote were represented by analytical functions. The long-range interaction potential is dominated by electrostatic interactions, including the charge-induced dipole and charge-quadrupole interactions. A comparison between the analytical potential and the *ab initio* data indicated that the analytical PES provides an accurate representation of the long-range interactions. In Fig. 1(a), the reaction path for this reaction is illustrated, in which the barrierless exothermic reaction is shown to have a bottleneck in the entrance channel, featuring a submerged saddle point. Using this PES, rate coefficients for the  $\text{H}_2\text{O}^+ + \text{H}_2(\text{D}_2)$  reactions have been calculated using a quasi-classical trajectory (QCT) method, and the results agreed excellently with the experimental values between 100 and 600 K.<sup>23</sup> In addition, the dynamics of this prototypical ion-molecule reaction has also been investigated. Despite much progress in quantum reactive scattering recently,<sup>31</sup> full dimensional quantum mechanical characterization of the dynamics of this reaction is still beyond our reach. In our earlier work,<sup>25</sup> we have used a seven-dimensional quantum dynamics (QD) model to study the dynamics of the  $\text{H}_2\text{O}^+ + \text{H}_2(\text{D}_2)$  reactions, which reproduced well the experimentally observed rotational enhancement and vibrational inhibition effects.<sup>24,27</sup> These reduced-dimensional quantum mechanical results were reproduced satisfactorily by full-dimensional QCT studies. The rotational enhancement of

reactivity was successfully explained by the Sudden Vector Projection model,<sup>32</sup> which attributes the enhancement to the strong coupling of the rotational modes of  $\text{H}_2\text{O}^+$  with the reaction coordinate at the submerged saddle point.<sup>29</sup>

Although the theoretical results are in general consistent with the experimental findings, the calculated integral cross sections are smaller than the experimentally measured absolute cross sections.<sup>25</sup> The theory-experiment discrepancies could be due to the reduced-dimensional QD model and/or the neglect of the Coriolis coupling in the QD calculations. Uncertainties in experiments ( $\sim 50\%$ ) may also be responsible for the differences. On the other hand, the calculated rate coefficients were found to agree with the latest measurements very well in the entire experimental temperature range.<sup>23</sup>

Very recently, Ng and coworkers have reported the product branching ratios (BRs) of the  $\text{H}_2\text{O}^+ + \text{HD}$  reaction, which have been accurately determined with the uncertainty estimated to be  $\sim 5\%$ .<sup>26</sup> As commented by Xu *et al.*, since all experimental cross sections of different rovibrational states for the  $\text{H}_2\text{O}^+ + \text{HD}$  reaction can be measured under the same experimental conditions, the BRs for the formation of  $\text{H}_3\text{O}^+$  and  $\text{H}_2\text{DO}^+$  are expected to be highly reliable,<sup>26</sup> and can therefore be taken as benchmarks for first-principles QD and QCT calculations.

The knowledge of intra- and intermolecular isotope effects provides valuable insights into the effect of zero-point energies and quantum tunneling on molecular reaction dynamics. Indeed, the isotope effects on triatomic and tetra-atomic reactions have been extensively investigated.<sup>33–45</sup> In this work, the dynamics of the  $\text{H}_2\text{O}^+ + \text{HD}$  reaction will be studied using the initial state-selected time-dependent wave packet method within a reduced seven-dimensional model, in which the two non-reactive O–H bonds are fixed. This model should provide accurate characterization of the quantum dynamics. In addition, a full dimensional QCT method is also used for comparison. Particular attention will be paid to the competition between the H- and D-atom transfer channels and the calculated product BRs will be compared with the experimental values obtained recently. This paper is organized as follows. Section II outlines the theoretical methodology of both the initial state-selected time-dependent wave packet and QCT methods. The results and discussion are presented in Section III. We conclude in Section IV.

## II. Theory

### IIA. Quantum dynamics

The initial state-selected time-dependent wave packet method has been detailed in the literature.<sup>46</sup> Here, we only outline the specific aspects related to this work. The reduced seven-dimensional Hamiltonian with a given total angular momentum  $J_{\text{tot}}$  in the reactant Jacobi coordinates, as shown in Fig. 1(b), can be written as ( $\hbar = 1$  hereafter)

$$\hat{H} = -\frac{1}{2\mu_R} \frac{\partial^2}{\partial R^2} + \hat{h}_1(r_1) + \frac{(\hat{J}_{\text{tot}} - \hat{J})^2}{2\mu_R R^2} + \frac{\hat{j}_1^2}{2\mu_1 r_1^2} + \frac{\hat{l}_2^2}{2\mu_2 r_{20}^2} + \frac{\hat{j}_3^2}{2\mu_3 r_{30}^2} + \hat{V}(R, r_1, \theta_1, \theta_2, \theta_3, \varphi_1, \varphi_2) - V^{\text{ref}}(r_1), \quad (1)$$

where  $R$  is the distance between the centers of mass (COMs) of AB and CDE,  $r_1$  is the bond distance of AB,  $r_2$  is the distance from C to the COM of DE and  $r_3$  is the bond distance of DE.  $r_{20}$  and  $r_{30}$  are fixed at  $1.9281a_0$  and  $1.8881a_0$ , respectively. Since the O atom at position E is much heavier than the H atom at positions C and D, this constraint is approximately equivalent to fixing the two nonreactive OH bonds.  $\mu_R$ ,  $\mu_1$ ,  $\mu_2$ , and  $\mu_3$  are the corresponding reduced masses.  $\hat{j}_3$  is the rotational angular momentum operator of DE and  $\hat{l}_2$  is the orbital angular momentum operator of atom C with respect to DE.  $\hat{j}_{23}$  is the angular momentum operator of CDE, which is coupled by  $\hat{j}_3$  and  $\hat{l}_2$ .  $\hat{j}_1$  is the rotational angular momentum operator of AB.  $\hat{j}$  is the sum of  $\hat{j}_1$  and  $\hat{j}_{23}$ . The one-dimensional (1D) reference Hamiltonian  $\hat{h}_1(r_1)$  is defined as

$$\hat{h}_1(r_1) = -\frac{1}{2\mu_1} \frac{\partial^2}{\partial r_1^2} + V^{\text{ref}}(r_1), \quad (2)$$

where  $V^{\text{ref}}(r_1)$  is the corresponding 1D reference potential.

The parity ( $\varepsilon$ ) adapted wave function is expanded in terms of the body-fixed (BF) ro-vibrational basis functions:

$$\psi^{J_{\text{tot}} M \varepsilon}(\vec{R}, \vec{r}_1, \vec{r}_2, \vec{r}_3) = \sum_{n, v_1, j, K} F_{nv_1 j K}^{J_{\text{tot}} M \varepsilon} u_n^{v_1}(R) \phi_{v_1}(r_1) \Phi_{jK}^{J_{\text{tot}} M \varepsilon}(\hat{R}, \hat{r}_1, \hat{r}_2, \hat{r}_3), \quad (3)$$

where  $n$  labels the translational basis functions,  $v_1$  is the vibrational basis index along  $r_1$ ,  $j$  denotes  $(j_1, l_2, j_3, j_{23}, J)$ . The translational basis function,  $u_n^{v_1}$ , is dependent on  $v_1$  due to the use of an L-shaped grid.<sup>47</sup>  $\Phi_{jK}^{J_{\text{tot}} M \varepsilon}$  in eqn (3) is the parity-adapted coupled BF total angular momentum eigenfunction, which can be written as

$$\begin{aligned} \Phi_{jK}^{J_{\text{tot}} M \varepsilon} &= (1 + \delta_{K0})^{-1/2} \sqrt{\frac{2J_{\text{tot}} + 1}{8\pi}} \left[ D_{K,M}^{J_{\text{tot}}} Y_{j_1 j_2 j_3}^{JK} \right. \\ &\quad \left. + \varepsilon (-1)^{j_1 + l_2 + j_3 + J + J_{\text{tot}}} D_{-K,M}^{J_{\text{tot}}} Y_{j_1 j_2 j_3}^{J-K} \right], \end{aligned} \quad (4)$$

where  $D_{K,M}^{J_{\text{tot}}}$  is the Wigner rotation matrix.<sup>48</sup>  $M$  is the projection of  $J_{\text{tot}}$  on the space-fixed  $z$  axis, and  $K$  is its projection on the BF  $z$  axis that coincides with the Jacobi coordinate  $R$ . Note the restriction that  $\varepsilon(-1)^{j_1 + l_2 + j_3 + J + J_{\text{tot}}} = 1$  for  $K = 0$  in eqn (4).  $Y_{j_1 j_2 j_3}^{JK}$  is the eigenfunction of  $\hat{j}$ , which is defined as

$$Y_{j_1 j_2 j_3}^{JK} = \sum_{\omega} \langle j_1 \omega j_{23} K - \omega | JK \rangle y_{j_1 \omega}(\hat{r}_1) Y_{j_{23} l_2 j_3 K - \omega}(\hat{r}_2, \hat{r}_3), \quad (5)$$

where

$$Y_{j_{23} l_2 j_3 K - \omega}(\hat{r}_2, \hat{r}_3) = \sum_m D_{K-\omega}^{j_{23}}(\hat{r}_2) \sqrt{\frac{2l_2 + 1}{2j_{23} + 1}} \langle j_3 m l_2 0 | j_{23} m \rangle y_{j_3 m}(\hat{r}_3). \quad (6)$$

In eqn (6),  $\omega$  is the projection of  $j_1$  on the BF  $z$  axis and  $y_{jm}$  denotes the spherical harmonics.

Using the centrifugal-sudden (CS) approximation,<sup>49,50</sup> the centrifugal term, i.e.,  $(\hat{J}_{\text{tot}} - \hat{j})^2$  in the Hamiltonian, is approximated by

$$\begin{aligned} &\langle \Phi_{jK}^{J_{\text{tot}} M \varepsilon} | (\hat{J}_{\text{tot}} - \hat{j})^2 | \Phi_{j'K'}^{J_{\text{tot}} M \varepsilon} \rangle \\ &\approx \delta_{jj'} \delta_{KK'} [J_{\text{tot}}(J_{\text{tot}} + 1) + J(J + 1) - 2K^2]. \end{aligned} \quad (7)$$

The initial wave packet  $|\chi_i\rangle$  is constructed as the direct product of a localized Gaussian wave packet along the scattering coordinate  $R$  in the reactant asymptote and a specific ( $J_{\text{tot}} K \varepsilon$ ) state of the reactive system with specific internal ro-vibrational states of both HD and  $\text{H}_2\text{O}^+$ :

$$|\chi_i\rangle = \left( \frac{1}{\pi \delta^2} \right)^{1/4} e^{-(R-R_0)^2/2\delta^2} e^{-ik_i R} |\nu_{1i}\rangle |j_{1i} j_{23i} J_i K_i \tau; J_{\text{tot}} \varepsilon\rangle, \quad (8)$$

where  $R_0$ ,  $\delta$  and  $k_i$  are the mean position, width, and momentum of the Gaussian wave packet,  $j_{1i}$ ,  $j_{23i}$ ,  $J_i$  and  $K_i$  are the initial angular quantum numbers, and  $\tau$  is the parity of  $\text{H}_2\text{O}^+$ .  $k_i$  is given by  $E_i$  via  $k_i = \sqrt{2\mu_R E_i}$ . The initial ro-vibrational states of  $\text{H}_2\text{O}^+$  were obtained by diagonalizing its Hamiltonian. The triatomic Hamiltonian of  $\text{H}_2\text{O}^+$  with the two non-reactive OH bonds fixed at the equilibrium position can be written as

$$\hat{h}_{23} = \frac{\hat{l}_2^2}{2\mu_2 r_{20}^2} + \frac{\hat{j}_3^2}{2\mu_3 r_{30}^2} + \hat{V}(\theta_3). \quad (9)$$

The interaction potential  $V$  depends only on the coordinate  $\theta_3$  in the reactant asymptote.

The second order split-operator method<sup>51</sup> is employed to propagate the wave packet in time. The outgoing boundary conditions are imposed by applying a negative imaginary absorbing potential at the edge of the grid as follows:

$$D(x) = -i\alpha \left( \frac{x - x_a}{x_{\text{max}} - x_a} \right)^n, \quad (10)$$

where  $x = R$  and  $r_1$ ,  $x_a$  is the starting point for the absorption potential.

The total reaction probability from a specific initial state is calculated using a flux formula

$$P_{v_1 v_{\text{H}_2\text{O}^+} j_1 j_{23} J K}^{J_{\text{tot}} \varepsilon}(E) = \langle \chi_i^+(E) | \hat{F} | \chi_i^+(E) \rangle, \quad (11)$$

where the flux operator  $\hat{F} = \text{Im} \left[ \frac{1}{\mu_1} \delta(r_1 - r_1^F) \frac{\partial}{\partial r_1} \right]$ . The flux through the dividing surface,  $S[r_1 = r_1^F]$ , is obtained from the energy-dependent scattering wavefunction,  $\psi_i^+(E)$ , which is computed by Fourier transforming the time-dependent wave packet at the dividing surface. The initial state-selected integral cross section (ICS) is obtained by summing the reaction probabilities over all relevant partial waves (total angular momentum  $J_{\text{tot}}$ ),

$$\begin{aligned} \sigma_{v_1 v_{\text{H}_2\text{O}^+} j_1 j_{23}}(E) &= \frac{1}{(2j_1 + 1)(2j_{23} + 1)} \sum_{J K \varepsilon} \frac{\pi}{k^2} \\ &\times \sum_{J_{\text{tot}} \geq K} (2J_{\text{tot}} + 1) P_{v_1 v_{\text{H}_2\text{O}^+} j_1 j_{23} J K}^{J_{\text{tot}} \varepsilon}(E) \end{aligned} \quad (12)$$

where  $K$  is taken from 0 to  $\min(J, J_{\text{tot}})$ . In this study, we focus on the dynamics from the reactant ground rotational states, *i.e.*  $j_1 = j_{23} = 0$  and thus drop the rotational indices hereafter.

Since there exist two non-equivalent product channels in this reaction, the H- and D-transfer channels, it is crucial to separate the reactive flux. Unlike the conventional multi-channel reactions such as  $\text{H} + \text{H}_2\text{O}$  and  $\text{H} + \text{NH}_3$ ,<sup>52,53</sup> in which the exchange channel and the abstraction channel can be well distinguished according to the reactant Jacobi coordinates, it is not straightforward to separate the H- and D-transfer channels as they coincide in the reactant coordinates. In our calculations, an approximate “integration” procedure is implemented to collect the reactive flux in different channels.<sup>40</sup> Briefly, the time-independent wave function at a specific translational energy obtained in the finite basis representation (FBR) is first transformed into discrete variable representation (DVR):

$$\begin{aligned} P_{iE}^{\text{FBR}} &= \left\langle \chi_{iE}^{+, \text{FBR}} \left| \hat{F} \right| \chi_{iE}^{+, \text{FBR}} \right\rangle = \frac{1}{\mu_1} \text{Im} \left\langle \chi_{iE}^{+, \text{FBR}} \left| \frac{\partial}{\partial r_1} \right| \chi_{iE}^{+, \text{FBR}} \right\rangle \bigg|_{r_1=r_1^{\text{F}}} \\ &= \frac{1}{\mu_1} \text{Im} \left\langle \chi_{iE}^{+, \text{DVR}} \left| \frac{\partial}{\partial r_1} \right| \chi_{iE}^{+, \text{DVR}} \right\rangle \bigg|_{r_1=r_1^{\text{F}}} \\ &= \frac{1}{\mu_1} \text{Im} \left\langle \chi_{iE}^{+, \text{DVR}}(R, r_1^{\text{F}}, r_{20}, r_{30}, \theta_1, \theta_2, \theta_3, \varphi_1, \varphi_2) \right. \\ &\quad \times \left. \chi_{iE}^{+, \text{DVR}'}(R, r_1^{\text{F}}, r_{20}, r_{30}, \theta_1, \theta_2, \theta_3, \varphi_1, \varphi_2) \right\rangle = \sum_k P_k, \end{aligned} \quad (13)$$

where  $i$  denotes the initial state,  $E$  represents the translational energy and  $k$  is the index of the DVR basis. At each DVR point with a specific coordinate  $(R, \theta_1, \theta_2, \theta_3, \varphi_1, \varphi_2)$ , the bond distances of OH and OD (H and D are the atoms in the reactant HD) can be calculated. We then define evenly spaced grids for the two bond distances of OH and OD, for which their ranges are sufficiently large to cover all possible area. On the new double variable plane, each grid is denoted by  $g_m$ . For each DVR point  $k$ , the nearest grid point on the new double variable plane, marked as  $g_m$ , can be determined immediately according to the calculated bond distances of OH and OD. The probability at point  $g_m$  is computed by cumulating the probabilities projected to the point:

$$P_{g_m} = \sum_k P_{k \Rightarrow g_m} \quad (14)$$

Thus, we can obtain a probability distribution on the new double variable plane for each specific translational energy. The flux to the H-transfer channel is scattered in the upper triangular area with  $r_{\text{OH}} < r_{\text{OD}}$ , while the flux to the D-transfer channel falls into the lower triangular area with  $r_{\text{OD}} < r_{\text{OH}}$ . The probabilities of the two channels can be divided by collecting the flux in different areas.

The numerical parameters on an L-shaped grid are listed in Table 1. For the scattering coordinate  $R$ , 106 sine DVR basis functions/grid points are used in the entire range from 1.0 to 15.0  $a_0$  and 40 sine DVR grid points/basis functions are used in the interaction region. For the dissociating H–D bond of  $r_1$ , 24 potential optimized DVR (PODVR) grid points/basis functions are used in the interaction region, and 3 PODVR grid points/basis functions are

**Table 1** Numerical parameters used in the wave packet calculations. (Atomic units are used unless stated otherwise)

HD + H <sub>2</sub> O <sup>+</sup> → H + H <sub>2</sub> DO <sup>+</sup> /D + H <sub>3</sub> O <sup>+</sup>	
Grid/basis range and size:	$R \in [1.0, 15.0]$ $N_R^{\text{tot}} = 106, N_R^{\text{int}} = 40$ $N_{r_1}^{\text{int}} = 24, N_{r_1}^{\text{asy}} = 3$ $j_{1\text{max}} = 28, j_{23\text{max}} = 30, j_{3\text{max}} = 22$ $l_{2\text{max}} = 24, l_{3\text{max}} = 36$
Initial wave packet:	$R_0 = 12.0, \delta = 0.4, E_i = 0.25 \text{ eV}$
Damping term:	$R_a = 12.0, \alpha_R = 0.05, n_R = 2.5$ $r_{1a} = 4.0, \alpha_{r_1} = 0.035, n_{r_1} = 2.0$
Flux position:	$r_1^{\text{F}} = 3.5$

used in the asymptotic region. The propagation time is around 40 000 a.u. with a time step of 10 a.u.

## IIB. Quasi-classical trajectory method

Standard QCT calculations, implemented by the software VENUS,<sup>54</sup> were performed on the same PES. The initial vibrational state of the reactant H<sub>2</sub>O<sup>+</sup> was prepared by normal mode sampling. Since we are interested in the ground rotational state of H<sub>2</sub>O<sup>+</sup> in this work, the rotational temperature is taken to be zero, which assigns zero rotational energy about each axis. The ro-vibrational state of the H<sub>2</sub> reactant was sampled using the classical action-angle variables at an experimental temperature of 298 K.<sup>26</sup>

The total integral cross section (ICS) was computed by:

$$\sigma_{\text{r}}(E_{\text{T}}) = \pi b_{\text{max}}^2(E_{\text{T}}) P_{\text{r}}(E_{\text{T}}), \quad (15)$$

where the reaction probability at the specified collision energy  $E_{\text{T}}$  is given by the ratio between the number of reactive trajectories ( $N_{\text{r}}$ ) and the total number of trajectories ( $N_{\text{total}}$ ):

$$P_{\text{r}}(E_{\text{T}}) = N_{\text{r}}/N_{\text{total}} \quad (16)$$

The standard error is given by:  $\Delta = \sqrt{(N_{\text{total}} - N_{\text{r}})/N_{\text{total}} N_{\text{r}}}$ .

In the QCT calculations, the trajectories were launched with a reactant separation of 10.0 Å, and terminated when products reached a separation of 6.0 Å for reactive trajectories, or when reactants are separated by 10.0 Å for non-reactive trajectories. The central-difference algorithm was employed to calculate numerically the gradient during the propagation. The time step was chosen to be 0.02 fs. The total energy was conserved better than 0.04 kcal mol<sup>−1</sup> for most trajectories. A few trajectories which failed to converge energy to 0.04 kcal mol<sup>−1</sup> or were nonreactive after 4.0 ps were not counted in the final analysis. The maximal impact parameter ( $b_{\text{max}}$ ) was determined using small batches of trajectories with trial values and taken from 6.0 Å at 0.05 eV to 4.0 Å at 1.0 eV. 100 000 trajectories were run for each collision energy, with standard errors of these cross sections less than 1%.

## III. Results

Fig. 2 shows the calculated QD reaction probabilities for the formation of H<sub>3</sub>O<sup>+</sup> *via* H-transfer and H<sub>2</sub>DO<sup>+</sup> *via* D-transfer



from the  $\text{H}_2\text{O}^+(\text{X}^2\text{B}_1;000) + \text{HD}$  reaction with several selected total angular momentum values. The three quantum numbers in the parentheses denote the  $\text{H}_3\text{O}^+$  quantum numbers in its symmetric stretching, bending, and antisymmetric stretching modes, respectively. Clearly, the reaction probability of the H-transfer channel for lower  $J_{\text{tot}}$  partial waves is insensitive to the translational energy although there exist strong oscillations at low energies. In contrast, the probability of the D-transfer channel increases with the translational energy at relatively high energies. The oscillation behavior for both channels at low translational energies is probably caused by the pre-reaction well, which supports resonances. Overall, the D-transfer channel has a larger reaction probability than the H-transfer channel for lower  $J_{\text{tot}}$  partial waves over the energy range studied. As the  $J_{\text{tot}}$  increases, the H-transfer probability becomes larger than the D-transfer probability.

The corresponding QD integral cross sections, which are obtained by summing over the partial wave contributions, are presented in Fig. 3. For each channel the cross section first decreases sharply with the increase of translational energy except for some notable oscillations and then becomes nearly flat as the translational energy increases further. The translational energy dependence of the cross section is characteristic of a barrierless reaction.<sup>55</sup> The cross sections also indicate that the  $\text{H}_2\text{O}^+(\text{X}^2\text{B}_1;000) + \text{HD}$  reaction favors the formation of the product  $\text{H}_3\text{O}^+$  *via* H-transfer. Furthermore, the difference between the H- and D-transfer cross sections decreases with increasing translational energy. For translational energy values above 0.1 eV, the two channels exhibit very similar reactivities although the H-transfer cross section remains slightly larger than the D-transfer cross section. Therefore, it can be concluded that the  $\text{H}_2\text{O}^+ + \text{HD}$  reaction exhibits a very strong intramolecular isotope effect, especially at low translational energies. The QCT results are shown in the same figure for comparison, which reproduce the trend of the QD cross sections well.

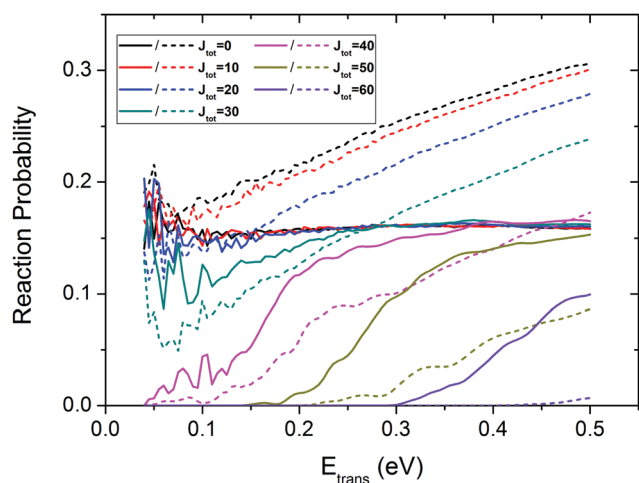


Fig. 2 Theoretical QD reaction probabilities for the  $\text{H}_2\text{O}^+(\text{X}^2\text{B}_1; 000) + \text{HD}$  reaction with several selected total angular momentum values. The solid lines denote the H-transfer channel and the dashed dotted lines represent the D-transfer channel.

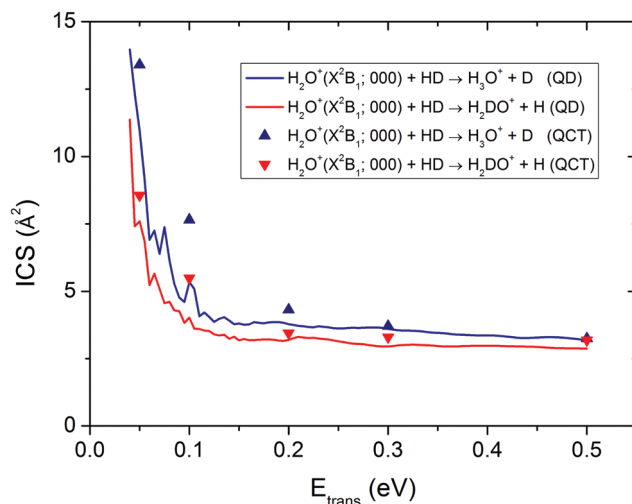


Fig. 3 Theoretical QD and QCT integral cross sections for the  $\text{H}_2\text{O}^+(\text{X}^2\text{B}_1; 000) + \text{HD}$  reaction.

The preference of the H-transfer channel from the excitation function of the  $\text{H}_2\text{O}^+(\text{X}^2\text{B}_1;000) + \text{HD}$  reaction differs somewhat from what is shown in Fig. 2, where the D-transfer probability is larger than the H-transfer probability for the low  $J_{\text{tot}}$  partial waves, indicating that higher  $J_{\text{tot}}$  partial waves play a more important role in the reaction cross sections. To clarify the contribution of the high  $J_{\text{tot}}$  partial waves to the excitation function, Fig. 4(a) presents the QD opacity functions at several translational energies:  $E_{\text{trans}} = 0.05, 0.2$  and  $0.5$  eV. The opacity functions show that the H-transfer channel favors larger impact parameter (or higher  $J_{\text{tot}}$ ) collisions, while the D-transfer channel prefers the smaller impact parameter collision. As the translational energy increases, the effective range of  $J_{\text{tot}}$  to the H-transfer reaction becomes wider than to the D-transfer channel. The preference of the H-transfer channel can thus be attributed to the contributions from the high  $J_{\text{tot}}$  partial waves.

The one-dimensional effective potentials along the reaction coordinate ( $s$ ), as plotted in Fig. 4(b), are employed to rationalize the observed dynamical behavior. The one-dimensional effective potential is defined as the sum of the potential energy along the minimum energy path and the centrifugal potential  $V_{\text{a}}^{J_{\text{tot}}}(s) = V_{\text{MEP}}(s) + J_{\text{tot}}(J_{\text{tot}} + 1)/2\mu R(s)^2$ . For low  $J_{\text{tot}}$  partial waves, both channels are dominated by the submerged barrier near the potential saddle point, while the centrifugal potential increases quickly for high  $J_{\text{tot}}$  values. Most importantly, for high  $J_{\text{tot}}$  collisions, the effective barrier for the H-transfer channel is substantially lower than that for the D-transfer channel, which suggests that the high  $J_{\text{tot}}$  collisions favor the formation of the  $\text{H}_3\text{O}^+$  product *via* H-transfer. This simple model provides an explanation for the behavior in the cross sections.

This behavior can also be explained from a different perspective. The intermolecular isotope effect in the  $\text{O}^+ + \text{HD}$  reaction has been studied by Martínez *et al.* using the QCT method.<sup>56</sup> Considering the similarity of the two reactions, it is interesting to compare the effect with what has been observed in the  $\text{H}_2\text{O}^+ + \text{HD}$  reaction. For the  $\text{O}^+ + \text{HD}$  reaction, the  $\text{OH}^+ + \text{D}$

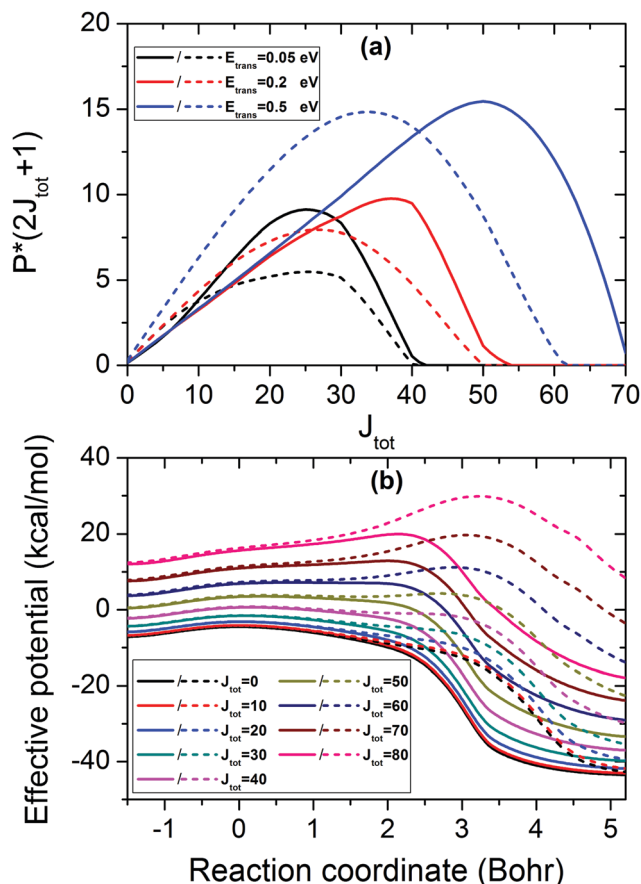


Fig. 4 (a) The QD opacity function for the  $\text{H}_2\text{O}^+(\text{X}^2\text{B}_1; 000) + \text{HD}$  reaction at several translational energies:  $E_{\text{trans}} = 0.05, 0.2$  and  $0.5$  eV. (b) One-dimensional effective potentials along the reaction coordinate at several selected values of the total angular momentum. The effective potential is defined as the sum of the minimum energy path and the centrifugal potential. The solid lines denote the H-transfer channel and the dashed dotted lines represent the D-transfer channel.

channel exhibits a larger cross section than the  $\text{OD}^+ + \text{H}$  channel when the translational energy lies below  $2.0$  eV. The difference first increases with the translational energy up to  $0.3$  eV and then decreases as the translational energy increases further. The  $\text{H}_2\text{O}^+$  cation in our case can be reasonably approximated as a slightly heavier oxygen cation. According to a kinematical model,<sup>34</sup> the  $\text{O}^+ - \text{H}$  collision occurs at a longer relative distance than the  $\text{O}^+ - \text{D}$  one, leading to a smaller centrifugal potential for a given impact parameter and therefore allowing larger impact parameter collisions. In contrast, the larger cone of acceptance of the  $\text{O}^+ - \text{D}$  attack than the  $\text{O}^+ - \text{H}$  one accounts for the larger reaction probability of the  $\text{O}^+ - \text{D}$  channel for smaller impact parameter collisions.

The experimental BRs for the H- and D-transfer channels of the  $\text{H}_2\text{O}^+(\text{X}^2\text{B}_1; 000) + \text{HD}$  reaction were determined by Ng and coworkers with an assigned uncertainty of  $\sim 5\%$ .<sup>26</sup> The comparison of theoretical and experimental BRs of the  $\text{H}_2\text{O}^+(\text{X}^2\text{B}_1; 000) + \text{HD}$  reaction is given in Fig. 5(a). For translational energies of  $0.05, 0.2, 0.3, 0.4$ , and  $0.5$  eV, the theoretical BRs agree well with the experimental values. However, the experimental BRs show that the strongest intramolecular isotope effect occurs at

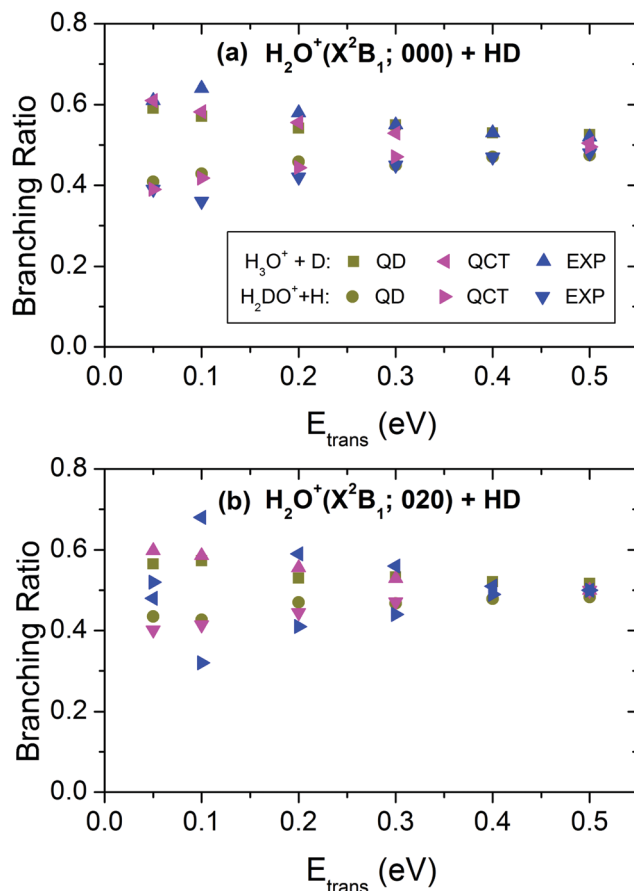


Fig. 5 Comparison of the theoretical and experimental branching ratios for the formation of  $\text{H}_3\text{O}^+$  via H-transfer ( $\sigma_{\text{HT}}/(\sigma_{\text{HT}} + \sigma_{\text{DT}})$ ) and for the formation of  $\text{H}_2\text{DO}^+$  via D-transfer ( $\sigma_{\text{DT}}/(\sigma_{\text{HT}} + \sigma_{\text{DT}})$ ) of (a) the  $\text{H}_2\text{O}^+(\text{X}^2\text{B}_1; 000) + \text{HD}$  reaction and (b) the  $\text{H}_2\text{O}^+(\text{X}^2\text{B}_1; 020) + \text{HD}$  reaction.  $\sigma_{\text{HT}}$  denotes the H-transfer cross section and  $\sigma_{\text{DT}}$  represents the D-transfer cross section.

$E_{\text{trans}} = 0.1$  eV, while the theoretical BRs indicate that the isotope effect increases monotonically with decreasing translational energy. Importantly, the QD and QCT BRs are in good agreement with each other. However, it is still infeasible to predict conclusively the dominant channel at lower collision energies as the theoretical and experimental BRs present different dependences on the collision energy.

Ng and coworkers have also investigated the vibrational mode specificity of the  $\text{H}_2\text{O}^+ + \text{HD}$  reaction and its influence on the intramolecular isotope effect.<sup>26</sup> It was reported that the excitation of the symmetric stretching mode of  $\text{H}_2\text{O}^+$  promotes the reaction in the  $0.03$ – $10.00$  eV range while the bending excitation leads to an inhibitory effect at very low collision energies. These results were quite surprising, as for the  $\text{H}_2\text{O}^+ + \text{H}_2(\text{D}_2)$  reactions, excitations of either the symmetric stretching mode or the bending mode of  $\text{H}_2\text{O}^+$  inhibit the reaction and this effect was observed in both experimental and theoretical studies.<sup>24,25</sup> The current seven-dimensional QD model, in which the two non-reactive OH bonds in  $\text{H}_2\text{O}^+$  are fixed, can only describe the bending motion of  $\text{H}_2\text{O}^+$  but not the symmetric stretching motion. Hence, we discuss only the effect of bending

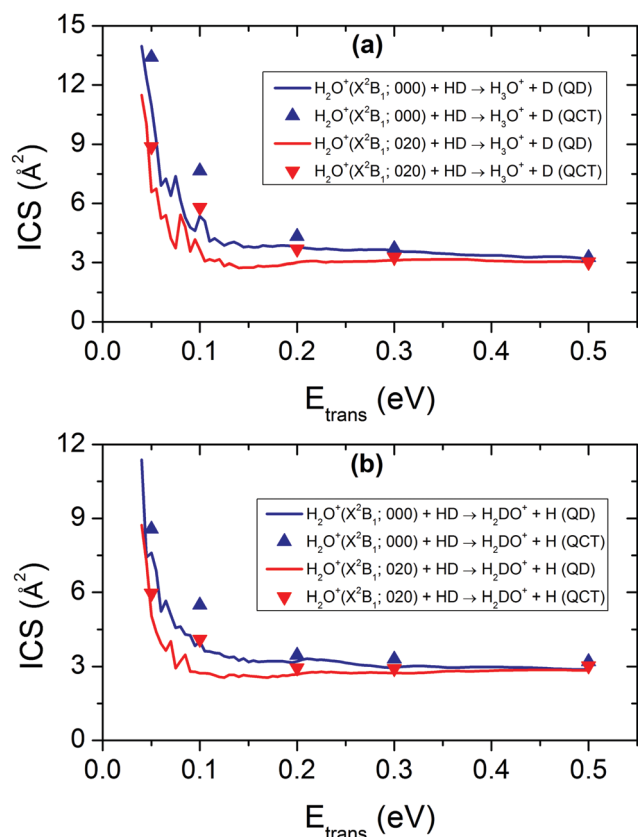


Fig. 6 (a) Theoretical QD and QCT integral cross sections for the  $\text{H}_2\text{O}^+(\text{X}^2\text{B}_1; 000, 020) + \text{HD} \rightarrow \text{H}_3\text{O}^+ + \text{D}$  reaction; and (b) theoretical QD and QCT integral cross sections for the  $\text{H}_2\text{O}^+(\text{X}^2\text{B}_1; 000, 020) + \text{HD} \rightarrow \text{H}_2\text{DO}^+ + \text{H}$  reaction.

excitations. Fig. 6 shows the QD and QCT integral cross sections for the  $\text{H}_2\text{O}^+(\text{X}^2\text{B}_1; 000, 020) + \text{HD}$  reaction. As can be seen from Fig. 6(a) for the H-transfer channel, both the QD and QCT calculations exhibit a clear inhibitory effect when the bending mode is excited. The inhibitory effect diminishes as the translational energy increases. For the D-transfer channel, as shown in Fig. 6(b), the effect of the bending mode excitation is similar to that in the H-transfer channel. By contrast, the experimental data suggest that for both the H-transfer and D-transfer channels excitation of the bending mode hinders the reaction only at very low collision energies, but enhances the reaction as the collision energy increases, and finally becomes ineffective. The reason for the inconsistency in the efficiency of the bending mode excitation in the moderate collision energy range is not clear. Theoretically, the reduced dimensional nature of our QD model and the neglect of the Coriolis coupling could lead to significant quantitative errors. However, the trends in the reduced-dimensional QD results are largely reproduced by full-dimensional QCT data, and a similar inhibitory effect was found in the  $\text{H}_2\text{O}^+ + \text{H}_2/\text{D}_2$  reactions. On the other hand, the uncertainty in the experimental measurements could not be completely ruled out as well due to the significantly lower PFI-PI intensity of  $\text{H}_2\text{O}^+(\text{X}^2\text{B}_1; 020)$  that can be prepared.

The calculated BRs of the  $\text{H}_2\text{O}^+(\text{X}^2\text{B}_1; 020) + \text{HD}$  reaction are presented in Fig. 5(b), together with the experimental values.

The agreement between the theoretical and experimental BRs is not as good as in the  $\text{H}_2\text{O}^+(\text{X}^2\text{B}_1; 000) + \text{HD}$  reaction although the QD and QCT BRs are largely consistent with each other. Overall, both the theoretical and experimental results indicate that the  $\text{H}_2\text{O}^+(\text{X}^2\text{B}_1) + \text{HD}$  reaction prefers to form the product  $\text{H}_3\text{O}^+$  *via* H-transfer. However, theoretical calculations could not reproduce the maximal isotope effect observed using the experiment at  $E_{\text{trans}} = 0.1$  eV, similar to the case for vibrational unexcited  $\text{H}_3\text{O}^+$  discussed above.

## IV. Conclusions

In this work, the reaction dynamics of  $\text{H}_2\text{O}^+(\text{X}^2\text{B}_1) + \text{HD}$  has been studied using a reduced seven-dimensional time-dependent wave packet method on an accurate global PES. Quasi-classical trajectory calculations were also carried out on the same PES to complement the quantum dynamics results. Both QD and QCT cross sections indicate that the  $\text{H}_2\text{O}^+(\text{X}^2\text{B}_1) + \text{HD}$  reaction prefers the H-transfer channel to the D-transfer channel. This theoretical trend is in good agreement with the latest experimental observations. The difference between the H- and D-transfer cross sections is found to decrease monotonically with increasing translational energy. This theoretical result differs somewhat from the experimental results, in which the branching ratio first increases and then decreases. The one-dimensional effective potential analysis shows that the bottleneck of the reaction is the submerged barrier at the transition state for lower  $J_{\text{tot}}$  partial waves, while it becomes the centrifugal potential for higher  $J_{\text{tot}}$  partial waves. The preference of the H-transfer channel to the D-transfer channel is hence caused by the high  $J_{\text{tot}}$  collisions, *i.e.*, with large impact parameters. Our theoretical results indicated that the vibrational excitation of the bending mode of  $\text{H}_2\text{O}^+$  inhibits the reaction. This inhibition effect was only observed experimentally at very low collision energies.

The detailed quantum mechanical and quasi-classical studies of this prototypical ion-molecule reaction provide important microscopic details of its dynamics. Despite the barrierless and exothermic nature of the reaction, the existence of a submerged saddle point near the entrance channel potential energy surface results in complex and surprising behaviors in mode specificity and isotope effects, as demonstrated here and in our earlier studies.

## Acknowledgements

H. S. and M. Y. were supported by the National Natural Science Foundation of China (Grant No. 21603266 to HS and 21373266 to MY) and H. G. acknowledges support by the Air Force Office of Scientific Research (Grant No. AFOSR-FA9550-15-1-0305). We thank Cheuk Ng and Al Viggiano for many stimulating discussions.

## References

- 1 J. Farrar, in *Springer, Handbook of Atomic, Molecular, and Optical Physics*, ed. G. Drake, Springer New York, New York, NY, 2006, pp. 983–993.
- 2 D. Smith, *Chem. Rev.*, 1992, **92**, 1473–1485.

- 3 N. S. Shuman, D. E. Hunton and A. A. Viggiano, *Chem. Rev.*, 2015, **115**, 4542–4570.
- 4 A. Fridman, *Plasma Chemistry*, Cambridge University Press, Cambridge, 2012.
- 5 J. Lequeux and E. Roueff, *Phys. Rep.*, 1991, **200**, 241–299.
- 6 D. Smith and P. Spanel, *Mass Spectrom. Rev.*, 1995, **14**, 255–278.
- 7 E. Herbst and W. Klemperer, *Astrophys. J.*, 1973, **185**, 505–533.
- 8 W. D. Watson, *Acc. Chem. Res.*, 1977, **10**, 221–226.
- 9 H. David, M. J. Kaufman, D. Neufeld, M. Wolfire and J. R. Goicoechea, *Astrophys. J.*, 2012, **754**, 105.
- 10 Y. Aikawa, N. Ohashi, S.-i. Inutsuka, E. Herbst and S. Takakuwa, *Astrophys. J.*, 2001, **552**, 639–653.
- 11 P. Caselli, C. M. Walmsley, A. Zucconi, M. Tafalla, L. Dore and P. C. Myers, *Astrophys. J.*, 2002, **565**, 344–358.
- 12 P. Caselli, F. F. S. van der Tak, C. Ceccarelli and A. Bacmann, *Astron. Astrophys.*, 2003, **403**, L37–L41.
- 13 C. Vastel, T. G. Phillips and H. Yoshida, *Astrophys. J., Lett.*, 2004, **606**, L127–L130.
- 14 F. Dong and D. J. Nesbitt, *J. Chem. Phys.*, 2006, **125**, 144311.
- 15 D. A. Kubose and W. H. Hamill, *J. Am. Chem. Soc.*, 1963, **85**, 125–127.
- 16 F. C. Fehsenfeld, A. L. Schmeltekopf and E. E. Ferguson, *J. Chem. Phys.*, 1967, **46**, 2802–2808.
- 17 A. G. Harrison and J. C. J. Thynne, *Trans. Faraday Soc.*, 1968, **64**, 945–953.
- 18 J. K. Kim, L. P. Theard and W. T. Huntress, *J. Chem. Phys.*, 1975, **62**, 45–52.
- 19 I. Dotan, W. Lindinger, B. Rowe, D. W. Fahey, F. C. Fehsenfeld and D. L. Albritton, *Chem. Phys. Lett.*, 1980, **72**, 67–70.
- 20 A. B. Rakshit and P. Warneck, *J. Chem. Soc., Faraday Trans. 2*, 1980, **76**, 1084–1092.
- 21 A. B. Rakshit and P. Warneck, *J. Chem. Phys.*, 1981, **74**, 2853–2859.
- 22 J. D. C. Jones, K. Birkinshaw and N. D. Twiddy, *Chem. Phys. Lett.*, 1981, **77**, 484–488.
- 23 S. G. Ard, A. Li, O. Martinez, N. S. Shuman, A. A. Viggiano and H. Guo, *J. Phys. Chem. A*, 2014, **118**, 11485–11489.
- 24 Y. Xu, B. Xiong, Y. C. Chang and C. Y. Ng, *J. Chem. Phys.*, 2013, **139**, 024203.
- 25 H. Song, A. Li, H. Guo, Y. Xu, B. Xiong, Y. C. Chang and C. Y. Ng, *Phys. Chem. Chem. Phys.*, 2016, **18**, 22509–22515.
- 26 Y. Xu, B. Xiong, Y. C. Chang and C. Y. Ng, *Phys. Chem. Chem. Phys.*, 2017, **19**, 8694–8705.
- 27 Y. Xu, B. Xiong, Y. C. Chang and C. Y. Ng, *J. Chem. Phys.*, 2012, **137**, 241101.
- 28 A. Li, Y. Li, H. Guo, K.-C. Lau, Y. Xu, B. Xiong, Y.-C. Chang and C. Y. Ng, *J. Chem. Phys.*, 2014, **140**, 011102.
- 29 A. Li and H. Guo, *J. Chem. Phys.*, 2014, **140**, 224313.
- 30 B. Jiang, J. Li and H. Guo, *Int. Rev. Phys. Chem.*, 2016, **35**, 479–506.
- 31 D. H. Zhang and H. Guo, *Annu. Rev. Phys. Chem.*, 2016, **67**, 135–158.
- 32 H. Guo and B. Jiang, *Acc. Chem. Res.*, 2014, **47**, 3679–3685.
- 33 K. Tsukiyama, B. Katz and R. Bersohn, *J. Chem. Phys.*, 1985, **83**, 2889–2893.
- 34 G. W. Johnston, H. Kornweitz, I. Schechter, A. Persky, B. Katz, R. Bersohn and R. D. Levine, *J. Chem. Phys.*, 1991, **94**, 2749–2757.
- 35 J. B. Song and E. A. Gislason, *J. Chem. Phys.*, 1993, **99**, 5117–5125.
- 36 F. J. Aoiz, L. Bañares, V. J. Herrero, V. Sáez Rábanos, K. Stark and H. J. Werner, *J. Chem. Phys.*, 1995, **102**, 9248–9262.
- 37 D. Skouteris, D. E. Manolopoulos, W. Bian, H.-J. Werner, L.-H. Lai and K. Liu, *Science*, 1999, **286**, 1713–1716.
- 38 M.-D. Chen, B.-Y. Tang, K.-L. Han and N.-Q. Lou, *Chem. Phys. Lett.*, 2001, **337**, 349–354.
- 39 R. A. Sultanov and N. Balakrishnan, *J. Chem. Phys.*, 2004, **121**, 11038–11044.
- 40 H. Song, Y. Lu and S.-Y. Lee, *J. Chem. Phys.*, 2011, **135**, 014305.
- 41 B. Fu and D. H. Zhang, *J. Chem. Phys.*, 2015, **142**, 064314.
- 42 H. Song and H. Guo, *J. Chem. Phys.*, 2015, **142**, 174309.
- 43 H. Song, S.-Y. Lee, Y. Lu and H. Guo, *J. Phys. Chem. A*, 2015, **119**, 12224–12230.
- 44 R. B. Bernstein, D. R. Herschbach and R. D. Levine, *J. Phys. Chem.*, 1987, **91**, 5365–5377.
- 45 C. E. Dateo and D. C. Clary, *J. Chem. Soc., Faraday Trans. 2*, 1989, **85**, 1685–1696.
- 46 J. Z. H. Zhang, *Theory and Application of Quantum Molecular Dynamics*, World Scientific, Singapore, 1999.
- 47 D. H. Zhang and J. Z. H. Zhang, *J. Chem. Phys.*, 1993, **99**, 5615–5618.
- 48 R. N. Zare, *Angular Momentum*, Wiley, New York, 1988.
- 49 R. T. Pack, *J. Chem. Phys.*, 1974, **60**, 633–639.
- 50 P. McGuire and D. J. Kouri, *J. Chem. Phys.*, 1974, **60**, 2488–2499.
- 51 M. D. Feit, J. A. Fleck Jr and A. Steiger, *J. Comput. Phys.*, 1982, **47**, 412–433.
- 52 D. H. Zhang, M. A. Collins and S.-Y. Lee, *Science*, 2000, **290**, 961–963.
- 53 H. Song, M. Yang and H. Guo, *J. Chem. Phys.*, 2016, **145**, 131101.
- 54 W. L. Hase, R. J. Duchovic, X. Hu, A. Komornicki, K. F. Lim, D.-H. Lu, G. H. Peslherbe, K. N. Swamy, S. R. V. Linde, A. Varandas, H. Wang and R. J. Wolf, *Quantum Chem. Program Exch. Bull.*, 1996, **16**, 671.
- 55 H. Guo, *Int. Rev. Phys. Chem.*, 2012, **31**, 1–68.
- 56 R. Martínez, J. D. Sierra and M. González, *J. Chem. Phys.*, 2005, **123**, 174312.